

A scalable and resilient protection framework for hybrid microgrids using zero injection cluster and graph learning

Awagan Goyal Ramesh Rao^{a,*}, Jing Jiang^a , Ebha Koley^b , Subhojit Ghosh^b , Pratik Harsh^c , Hongjian Sun^c

^a Department of Mathematics, Physics & Electrical Engineering, Northumbria University, Ellison Pl, Newcastle Upon Tyne, NE1 8ST, United Kingdom

^b Department of Electrical Engineering, National Institute of Technology Raipur, GE Road, Raipur, 492010, Chhattisgarh, India

^c Department of Engineering, Durham University, Stockton Road, Durham, DH1 3LE, United Kingdom

HIGHLIGHTS

- Scalable protection framework for hybrid microgrids using graph learning approach.
- Critical sensor identification considering the effect of zero injection cluster.
- Modeling of solar and wind intermittency using joint probabilistic approach.
- Resilience against N-1 contingency scenarios caused by extreme weather events.
- Spatiotemporal graph convolutional network classifier modules for protection tasks.

ARTICLE INFO

Keywords:

Critical sensor identification
Hybrid microgrid
Joint probability distribution
N-1 contingency
Spatiotemporal graph convolutional network
Zero injection cluster

ABSTRACT

Hybrid microgrids in spite of offering a promising solution to meet rising energy demands, have not received wider acceptance by power utilities because of the complexity of their protection schemes. Real-world microgrids are highly susceptible to disruptions, during extreme weather conditions resulting in frequent line outages and sensor failures. Further complications arise from the variations in operational dynamics caused by weather dependent intermittent behavior of solar and wind distributed energy resources (DERs). Failing to address these issues, hinders accurate fault detection/classification under extreme weather conditions, thereby impacting the microgrid resilience. In this regard, a protection framework using zero injection cluster (ZIC) and graph learning with resilience against contingency scenarios and weather intermittency is proposed for the hybrid microgrid. The present work incorporates the effect of ZIC to formulate the critical sensor identification problem with the aim of minimizing sensor installation costs while enhancing measurement redundancy. The same imparts scalability to the protection scheme with regard to the architecture and size of the microgrid. To accommodate intermittency and potential correlations between solar and wind DERs, a joint probabilistic approach, encompassing the uncertainty present in both sources is considered. This work employs a spatiotemporal graph convolutional network classifier to detect and classify faults by integrating the network topology information into the protection framework. Validation of the proposed scheme for varying fault and operating scenarios reveals its ability to attain high degree of accuracy in fault detection and classification with increased resilience and immunity.

1. Introduction

Incorporating the microgrid concept into the current distribution grid aims to enhance the way renewable distributed energy resources (DERs) are integrated to deliver clean and sustainable electrical energy directly to consumers. Over time, advancements in

technology have facilitated the widespread deployment of solar and wind DERs into the microgrids. This transition has contributed significantly to fostering sustainable economic growth and development [1,2]. Microgrids are commonly categorized as AC, DC, or hybrid systems [3]. Considerable attention has been devoted to the AC microgrids due to

* Corresponding author.

Email address: goyal.awagan@northumbria.ac.uk (A. Goyal Ramesh Rao).

their straightforward design and the simplicity with which DERs can be integrated into the pre-existing AC utility grid with minimal modifications. Despite the long-standing presence of AC microgrids, they still face limitations concerning reactive power circulation and the requirement for DER synchronization. Despite the existence of AC microgrid from a very long time, it has certain limitations of the reactive power circulation and the need for synchronization of DERs. Conversely, DC microgrids have gained prominence in the distribution network owing to their enhanced efficiency and seamless integration with DC DERs. Nonetheless, the necessity for substantial modifications to the current distribution system, coupled with increased overall costs, often renders the deployment of a pure DC microgrid impractical. Hybrid microgrids, which feature a combination of AC and DC microgrid architecture, are gaining traction due to their versatility in directly integrating both AC and DC DERs, loads, and energy storage devices. This eliminates the need for multi-stage AC-DC and DC-AC conversions, leading to enhanced operational efficiencies and cost savings [4,5].

While hybrid microgrids present several benefits compared to AC and DC microgrids, their broader adoption and practical feasibility are significantly hindered by technical challenges associated with ensuring protection against line faults [6]. Interconnecting AC and DC sub-grids that have differing characteristics presents practical difficulties for precise fault detection and classification. The direct applicability of protection algorithms designed for AC microgrids to hybrid microgrids encounters several obstacles. These include the lack of zero-crossing, the unipolar characteristics of waveforms, and the need for a robust grounding mechanism. Likewise, the alternating characteristics of the signals derived from sensors in the AC microgrids render the protection algorithms for the DC microgrid inapplicable. Moreover, the variation in short-circuit current levels in different microgrid operating modes (grid-connected and islanded) contributes to the intricacy of the protection scheme [7]. Changes in the network topology caused by unwanted DER connections/disconnections, line outages and load changes further complicate the protection task. Additionally, the stochastic behavior of solar and wind DERs which depends on weather conditions, significantly influences the performance of the protection algorithm [8].

The literature currently reports relatively few hybrid microgrid protection schemes [4,7,9,10]. The review studies conducted in references [4,7] delve into challenges and potential future directions in the area of hybrid microgrid protection. The work reported in [9], developed a protection scheme for hybrid microgrids featuring a low-bandwidth communication infrastructure. It aimed to minimize communication delays and enhance immunity against converter faults. Also, the research outlined in [10], has formulated a protection scheme for identifying high impedance faults within hybrid microgrids. It offers resilience against solar irradiance intermittency and remains robust during N-1 line contingencies.

Microgrid protection schemes in the literature predominantly assume a fixed network topology. However, real-world microgrids are highly susceptible to disruptions, during extreme weather conditions, such as heatwaves or freezing temperatures. These events often lead to line outages and sensor failures, resulting in network topology changes. In power networks, scenarios resulting from component failures are commonly referred to as contingencies in industry standards. The literature widely discusses two types of contingencies i.e. line outage contingency and sensor loss contingency [11,12]. The N-1 contingency criterion is widely studied in power systems because it addresses the most common and frequently occurring failure scenarios. In accordance with the NERC (North American Reliability Corporation) standards, N-1 contingency is defined as the loss of any line (excluding radial lines), a source of generation or critical sensor [13]. To enhance microgrid resilience against extreme climate hazards, it is crucial to account for all practical contingencies when designing the protection algorithm. The only work reported in [10] focuses on enhancing the immunity of microgrid protection schemes and ensuring their adaptability to changes in network topology caused by N-1 line contingencies. One of the studies referenced

in [14] provides a comprehensive review of state-of-the-art strategies employing microgrids to enhance the resilience of power networks. To the best of the author's knowledge, none of the studies in the literature on hybrid microgrid protection have aimed to provide immunity against contingency scenarios arising from either a single line outage or a single sensor loss. Apart from contingency events, the performance of the protection scheme is also hindered by the vulnerability of solar and wind DERs to weather conditions. As of now, the only work reported in [10] has incorporated the solar irradiance intermittency into the framework of hybrid microgrid protection. There is, however, no work that incorporates both solar irradiance and wind speed intermittency into the hybrid microgrid protection algorithms.

Upon reviewing the existing body of research on hybrid microgrid protection, it becomes evident that none of the articles have addressed all the challenges in a comprehensive manner:

1. Applicability to microgrids of varying topologies and sizes.
2. Providing high degree of robustness against both line outages as well as sensor losses.
3. Incorporating the stochastic characteristics of solar as well as wind DERs with increased immunity against weather intermittency.

Considering the aforementioned issues, the aim of this paper is to develop a protection scheme for hybrid microgrid with improved resilience against contingency scenarios (i.e. single line outage or single sensor loss) and weather intermittency (i.e. solar irradiance and wind speed intermittency). Hence, a holistic framework leveraging a combined approach of joint probabilistic modeling and graph neural networks is developed for hybrid microgrid protection to enhance resilience against contingency scenarios and weather fluctuations.

To ensure high reliability and accuracy in protection, continuous monitoring of voltage and current signals is essential. This is achieved through sensors installed at relaying buses within the system. However, developing a protection strategy that incorporates real-time data from multiple sensors distributed across a large geographical area results in a significant increase in computational costs. Hence, it is crucial to identify a set of sensors (referred to as critical sensors) that guarantees system observability while minimizing the deployment costs associated with sensor installation. The set of such critical sensors contains the entire information regarding the network dynamics required for monitoring. In addition to the identification of the critical sensors, to avoid system failures during extreme weather conditions, it is necessary to ensure that the sensors have sufficient measurement redundancy. In this context, the critical sensor identification (CSI) task is framed as a constrained optimization problem that balances between two competing objectives: minimizing the costs associated with sensor deployment and maximizing measurement redundancy using the set of sensors obtained. While addressing the CSI problem, the impact of zero-injection buses (ZIBs), which is positively correlated with the number of reducible sensors, has been widely discussed in the literature [10,12,15]. The inclusion of zero-injection clusters (ZICs), defined as a set comprising a ZIB and all its incident buses helps to further optimize and reduce the number of required sensors. Some of the research works on optimal placement of phasor measurement units have used the concept of ZIC [16,17]. The present work also incorporates the effect of ZIC into the protection framework, aiming to minimize sensor installation costs while enhancing measurement redundancy for improved resilience against contingency events. The scalability with regard to accommodating different operating and contingency scenarios for a wider class of microgrid networks has been achieved by formulating the problem of selecting the critical sensor information using ZIC. The inclusion of all possible N-1 contingencies within the framework of ZIC allows for identifying the critical sensor locations, whose information would suffice for observability during both normal operations and contingency scenarios.

To account for the inherent intermittency of solar and wind power generation, the proposed protection scheme adopts a joint probabilistic approach that considers the uncertainty of solar irradiance and wind speed, and potential correlations that can be attributed to the microgrid's smaller geographical span. Probabilistic modeling has been implemented into the protection framework for AC and DC microgrids, but not yet for hybrid microgrids [18,19]. Utilizing the statistical co-variability between wind speed and solar irradiance, this article aims to develop a joint probability distribution model to execute protection tasks in the hybrid microgrid. By using the model and its joint probability, a range of different weather scenarios are incorporated to simulate various fault cases, considering all potential N-1 contingencies. Following this, the current signals collected from the sensors are fed into a graph neural network (GNN), a type of deep neural network classifier using graph-structured data to perform accurate fault detection and classification [20]. The literature reports on a variety of data-driven strategies employing deep learning architectures for fault diagnosis in microgrids [10,21]. However, the reported works have not embedded the microgrid system topology information during the training of the machine learning based protection algorithms. Unlike the traditional deep learning methods, GNN leverages the topological information inherent in microgrid networks during training, resulting in efficient feature extraction and strong generalization ability [22]. Some significant studies in the literature have used graph convolutional networks (GCN) to incorporate system topology information and post-fault data to carry out fault diagnosis in power transformers [23], transmission lines [24], and distribution systems [25]. In [26], a GCN-based approach has been adopted for detecting and classifying faults in low-voltage DC microgrids. Nevertheless, these methods still exhibit certain limitations. For instance, certain methods necessitate precise line parameter data, a requirement challenging to fulfill in real-world microgrids. Furthermore, GCN solely relies on spatial structural information, resulting in the extraction of less effective post-fault features [27]. In this context, the present study introduces a novel protection scheme for hybrid microgrids utilising a spatiotemporal graph convolutional network (STGCN) approach. Without requiring exact line parameters, the proposed graph-based approach incorporates microgrid network topology into the learning process of the protection algorithm. This results in capturing deeper structural information from the data, rendering it more resilient to faults, contingencies, and weather scenarios [28].

The major contributions/highlights of the proposed work can be summarized as follows:

1. Development of a scalable protection framework for hybrid microgrids using ZIC (for CSI task) and graph learning (for fault detection/classification task).
2. Formulation of the CSI problem which includes maintaining a trade-off between two competing objectives of minimizing sensor installation cost and maximizing measurement redundancy ensuring system observability to facilitate protection tasks.
3. Enhancing the resilience of hybrid microgrid protection against both line outages and sensor loss contingency scenarios resulting from extreme weather events.
4. Statistical modeling of solar and wind intermittency using time-series data, and the inclusion of the same in the hybrid microgrid protection scheme based on a probabilistic approach.

The remainder of the paper is structured as follows: Section 2 briefly describes the hybrid microgrid system under study. Section 3 presents the formulation of CSI problem using ZIC. Section 4 introduces probabilistic approach to model the solar irradiance and wind speed weather intermittency. The overview of GNN architecture and the framework of proposed STGCN-based protection scheme is discussed in Section 5. Section 6 validates the performance of the proposed protection scheme, while Section 7 presents the conclusion.

2. Hybrid microgrid system

The single-line diagram of the AC/DC hybrid microgrid system used in [10] is shown in Fig. 1. It includes two AC microgrids and one DC microgrid. The model incorporates DERs such as solar generator (725 kW), wind generator (10.5 kW) and diesel generator (DG) (3 MW) to supply electricity to the system's varied demands. The network is also equipped with two battery energy storage system i.e. BESS1 (three battery units of 1.5 Ah each) and BESS2 (single battery unit of 800 Ah). The model under study is linked to the main grid via a point of common coupling (PCC) at 69 kV and 60 Hz. In Fig. 1, the various components of the system are labelled as distribution lines (Z1, Z2, ..., Z14), buses (B-1, B-2, ..., B-17), converters (C-1, C-2, ..., C-6), loads (L2, L3, ..., DC Load), and transformers (T-1, T-2, ..., T-8). The detailed specifications of the components are available in [10].

3. Formulation of CSI problem using ZIC

The extensive geographical span of the hybrid microgrid system makes the installation of sensors at every bus both impractical and cost-prohibitive. To address this challenge, it is essential to identify a set of sensors that ensures system observability while minimizing deployment costs attributed to sensor installation. Maintaining observability is critical for effective monitoring of the system dynamics, enabling the timely detection and accurate classification of fault scenarios. As outlined earlier, for a given network topology, the voltage and current information from certain specific buses (referred to as critical buses) is sufficient to monitor the entire network and ensure its observability. The data acquired by the critical sensors installed at the critical buses contain the intricacies of the entire network dynamics required for monitoring. The CSI task is formulated as an optimization problem focused on minimizing the total cost of sensor installation and maximizing measurement redundancy, while ensuring network observability. Furthermore, the formulation incorporates the effect of ZIC, which can significantly reduce the required number of sensors.

The objective function for the CSI task under normal operating conditions, considering the effect of ZIC, can be framed using integer linear programming (ILP) as follows [29],

$$\text{Minimize } \sum_{i=1}^B c_{i(nom)} x_i - \sum_{i=1}^B R_i \quad (1)$$

$$\text{with } c_{i(nom)} = \frac{c_i}{\sum_{i=1}^B c_i}$$

$$\text{Subject to: } O_i = \sum_{j=1}^B p_{i,j} x_j - \sum_{z=1}^{B_z} p_{i,z} y_z - \sum_{\gamma=1}^{B_\gamma} p_{i,\gamma} x_\gamma \geq \psi \quad \forall i \in B \quad (2)$$

$$\sum_{i=1}^{\eta} p_{i,z} y_z \geq \eta - \eta_z - 1 \quad \forall z \in B_z \quad (3)$$

where, B denotes number of buses in the microgrid. In (1), $c_{i(nom)}$ is the normalized cost and c_i is the cost of sensor installation at Bus- i , x_i is the binary vector representing whether or not a sensor is installed at Bus- i and R_i denotes the redundancy of Bus- i

The two components ($\sum c_{i(nom)} x_i$ and $\sum R_i$) in the objective function (1) refers to two different objectives i.e. $\sum c_{i(nom)} x_i$ represents cost and $\sum R_i$ represents redundancy. In multi-objective optimization, multiple objectives with different units are combined by normalizing them to a common scale or by applying a suitable weighting factor. For the cost component in the present case, normalization has been carried out by dividing the total sensor installation cost $\sum_{i=1}^B c_i x_i$ (for a given configuration x_i) by the maximum cost (when the sensors are installed at all the buses with $x_i = \text{ones}(1, B)$) i.e. $c_1 + c_2 + c_3 + \dots + c_B$. Since x_i is a binary vector, $x_i \in \{0, 1\}$, the formulation of the objective function and

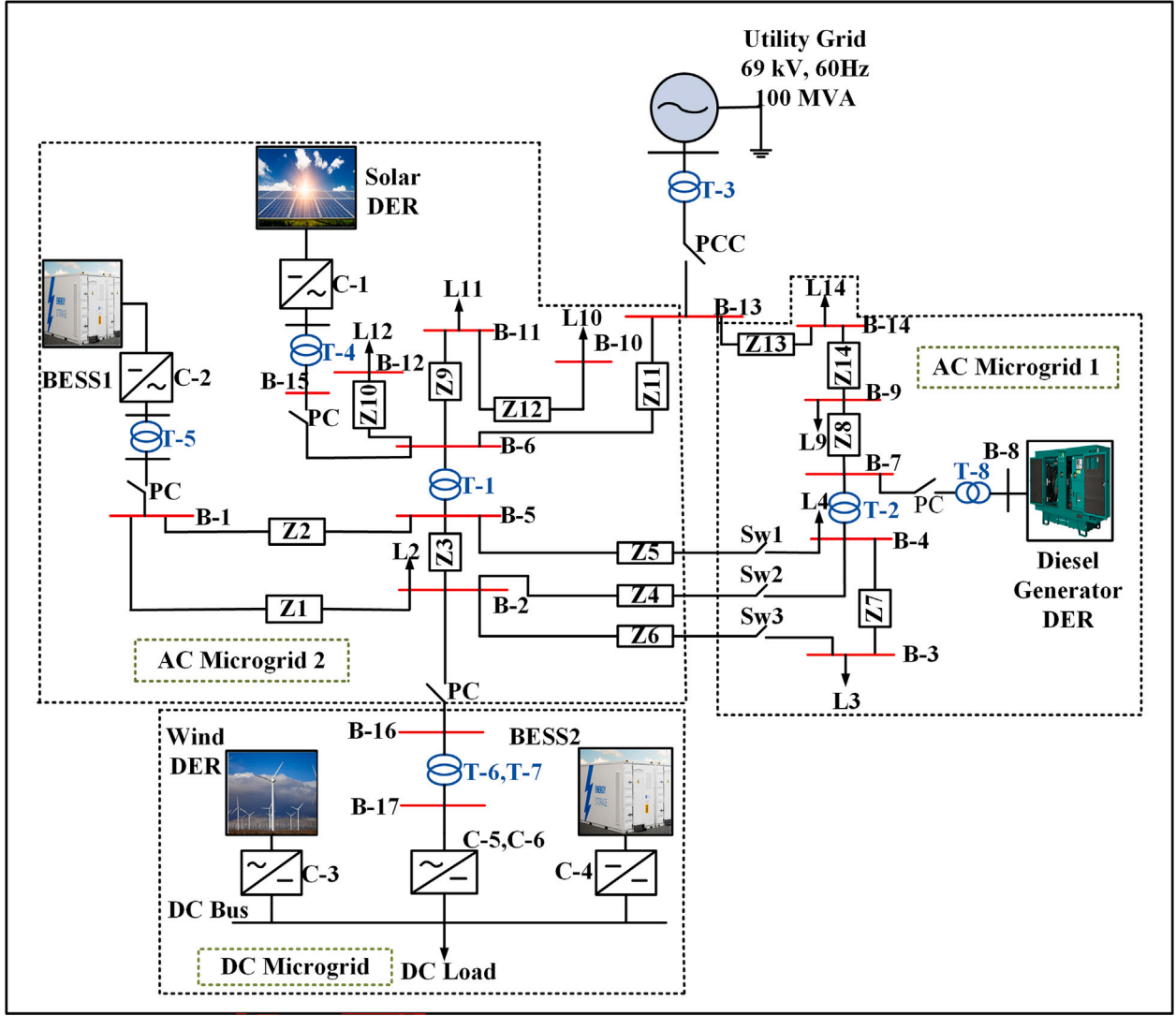


Fig. 1. Single line diagram of a hybrid microgrid system [10].

its solution does not require the specific values ($c_1, c_2, c_3, \dots, c_B$) of the sensor installation cost in dollars, euros or any other unit. Their normalized (unitless) values in the range of 0 to 1 can be used to minimize the objective function. In other words, the term $\sum c_{i(nom)} x_i$ provides a relative assessment regarding installation cost for different configurations of sensor installation x_i without quantifying the actual cost.

In (2), O_i denotes observability of Bus- i under normal operating conditions, $p_{i,j}$ is the entry of the connectivity matrix given as,

$$p_{i,j} = \begin{cases} 1 & \text{if } i = j \text{ or if Bus } -i \text{ is connected to Bus } -j \\ 0 & \text{otherwise} \end{cases} \quad (4)$$

The second term in (2) is included to account for the effect of ZIBs where, B_z denotes the number of ZIBs, $p_{i,z}$ is the binary variable equals 1 if i and z are connected; it is 0 otherwise and y_z denotes auxiliary variable to be added to each bus that belongs to ZIC. Similarly, the third term in (2) represents the effect of ZIB neighboring to ZIB- i where, $p_{i,\gamma}$ equals 1 if i and γ are connected and both are ZIBs; it is 0 if $i = \gamma$ or otherwise and x_γ denotes the ZIB neighboring to ZIB- i . Also ψ in (2) is the identity vector equals 0 if Bus- i is ZIB or Bus- i is connected to ZIB; 1 otherwise. Eq. (3) represents the constraint associated with the auxiliary variable where, η denotes the total number of buses within the ZIC, while η_z represents the number of neighboring ZIBs in the ZIC.

In the present work, the effect of a group of ZIBs {5,6} and a single ZIB {7} is considered to solve CSI problem. Under normal operating conditions, installing sensors at only five buses (2, 6, 9, 11, 16) renders the complete system observable as depicted in Fig. 2(a).

However, as previously mentioned, the microgrid system may experience network topology changes due to line outage contingencies or sensor loss contingencies during extreme weather events. This results in loss of sensor-based measurements affecting the overall system monitoring. In this regard, constraints ensuring post-contingency observability are incorporated into the present CSI problem and solved for N-1 contingency scenario (single sensor loss or single line outage). The objective function for CSI under contingency scenarios with ZIC remains identical to that in (1). However, the inequality constraint (2) needs to be re-framed to incorporate contingency cases as,

$$O_i^c = \sum_{j=1}^B p_{i,j} x_j - \sum_{\gamma=1}^{B_z} p_{i,\gamma} x_\gamma - \sum_{z=1}^{B_z} p_{i,z} y_z \geq 2\psi \quad \forall i \in B \quad (5)$$

In Eq. (5), O_i^c denotes observability of Bus- i under contingency scenarios.

Considering the possibility of single line outage contingency, sensors must be installed at bus locations 2, 4, 6, 9, 10, 11, 14, 16 and 17 whereas for single sensor loss it needs to be installed at bus locations

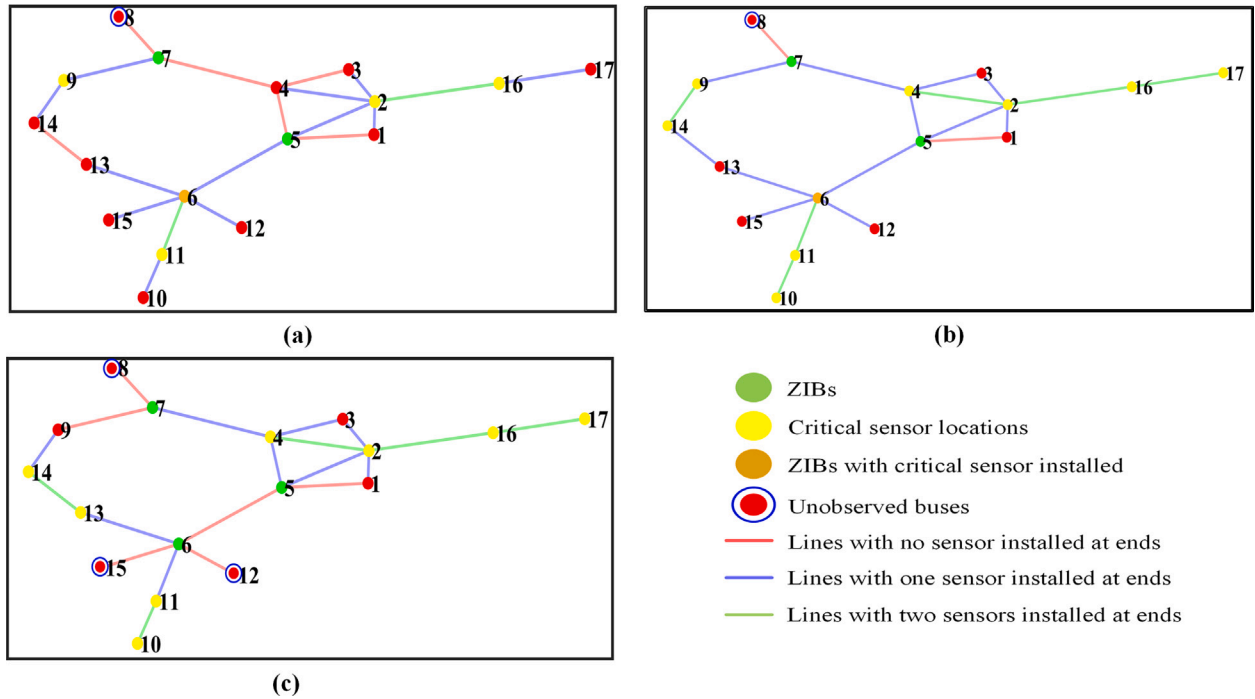


Fig. 2. Graphical Visualization of optimal sensor locations under (a) normal operating condition; (b) single line outage; (c) single sensor loss.

2, 4, 10, 11, 13, 14, 16 and 17 as depicted in Fig. 2(b) and (c) respectively to ensure that the system is fully observable.

The graphical visualization of optimal sensor locations derived for normal operating conditions, single line outage contingency and single sensor loss contingency is shown in Fig. 2. The sensors ensuring system observability are highlighted with yellow circles, ZIBs are marked with green circles, and a dark yellow circle represents a ZIB with an installed sensor. The external blue rings denote buses that cannot be directly observed by sensors but are observable through ZIBs. Lines with sensors installed at both ends are highlighted in green, while those with sensors at only one end are marked in blue. Additionally, lines that are not directly measured by sensors but are observable through ZIBs are shown in red. The proposed CSI approach achieves a substantial reduction in sensor installation costs, lowering them by approximately 71 % during normal operations and 41 % under N-1 contingency scenarios. The lines with sensors installed at both ends can be reached by two sensors (line redundancy 2). Hence, with the set of sensors obtained the proposed approach effectively balances the competing objectives of minimizing sensor installation costs and maximizing measurement redundancy.

4. Modeling of weather intermittency using probabilistic approach

Solar and wind DERs display sporadic patterns attributed to changes in irradiance levels and wind speeds. This weather-related unpredictability notably impacts the voltage–current characteristics within the microgrid system, which often leads to relay malfunctions. The current work aims to develop a protection scheme for hybrid microgrids, while considering the stochastic behavior of solar and wind DERs influenced by weather conditions. In this context, data sourced from National Renewable Energy Laboratory (NREL), specifically the National Solar Radiation Database (NSRDB), have been employed in the proposed microgrid model [30]. To accommodate renewable energy intermittency and potential correlations, the proposed protection scheme adopts a joint probabilistic approach, encompassing the uncertainty present in both variables. This statistical modeling will provide protection measures for the microgrid, ensuring reliability even in unpredictable

weather conditions. It will analyze historical weather patterns and integrate them into the protection system to anticipate potential risks and take proactive measures.

4.1. Joint probabilistic approach

Time-series historical data (annually recorded at hourly resolution), has been used to estimate the probability distribution functions for solar irradiance and wind speed variations. Initially, the fluctuation in irradiance levels is modeled using a Gaussian distribution function, while the uncertainty in wind speed is modeled using a Weibull distribution function. Furthermore, a joint probabilistic approach that considers the uncertainty in both variables is implemented.

4.1.1. Solar irradiance uncertainty modeling

The annual global horizontal irradiance (GHI) for the California region in the United States (US), recorded at hourly resolution for the year 2017, has been utilized [30]. These data were employed to model the intermittency in solar irradiance levels using a suitable probability distribution function (PDF), namely the Gaussian distribution function, because of its capability to mimic the behavior of solar irradiance fluctuations accurately over time. The randomness in the solar irradiance (100–1000 W/m²) is modeled in Fig. 3(a) by utilizing the normal Gaussian distribution function as [31],

$$f(g) = \frac{1}{\sqrt{2\pi}\sigma^2} \exp\left[-\frac{0.5(g - \mu)^2}{\sigma^2}\right] \quad (6)$$

where g denotes global horizontal irradiance (W/m²), μ represents mean of Gaussian distribution, and σ denotes standard deviation of Gaussian distribution.

4.1.2. Wind speed uncertainty modeling

Modeling wind speed uncertainty is facilitated by the Weibull distribution function due to its ability to encompass a diverse array of wind speed distributions across different geographic locations and under varying atmospheric conditions. Firstly, the annual wind speed data (ranging from 2 to 20 m/s) for the California region in the US is captured at an

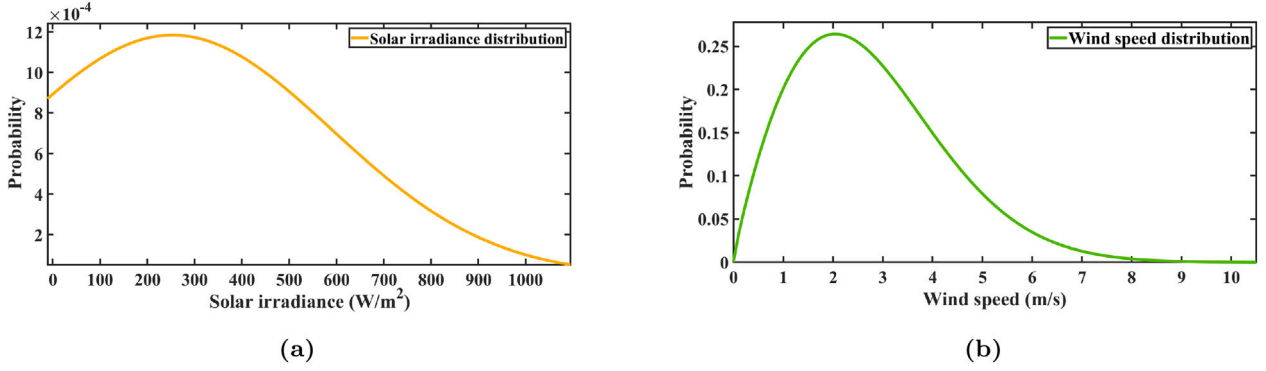


Fig. 3. Uncertainty model of (a) Solar irradiance; (b) Wind speed.

hourly precision [30]. The uncertainty in wind speed is represented in Fig. 3(b) through the Weibull distribution function as [31],

$$f(w) = \frac{\beta}{\alpha} \left(\frac{w}{\alpha}\right)^{\beta-1} \exp\left[-\left(\frac{w}{\alpha}\right)^\beta\right] \quad (7)$$

where w denotes the wind speed (m/s), α represents the scale parameter of the Weibull distribution, and β is the shape parameter of the Weibull distribution. The scale parameter determines the location of the distribution along the wind speed axis, while the shape parameter impacts the overall shape of the distribution curve.

4.1.3. Joint probability distribution model

Understanding the correlation or statistical relationship between solar irradiance and wind speed is of utmost importance in microgrids, particularly when evaluating the combined availability of solar and wind DERs. In this regard, historical data pertaining to specific locations has been analyzed, which indicate a complementary relationship between the two renewable energy sources. The overall impact of weather conditions on the performance of microgrid protection algorithms for a certain geographical region due to proximity of solar and wind DERs can be represented using a two-dimensional joint probability model. The proposed joint probabilistic approach is formulated utilizing the individual PDFs (6) and (7), representing solar irradiance and wind speed uncertainty. With solar irradiance and wind speed assumed to have discrete values, i.e. $g_m = g_1, g_2, \dots, g_q$ and $w_n = w_1, w_2, \dots, w_r$, the joint probability of occurrence can be expressed as,

$$P(g_m | w_n) = \frac{f(g_m \cap w_n)}{\sum_{m=1}^q f(w_{mn})} \begin{cases} 1 \leq m < q \\ 1 \leq n < r \end{cases} \quad (8)$$

$$[P(g_m | w_n)] = \begin{bmatrix} \frac{f(g_1 \cap w_1)}{\sum_{m=1}^q f(w_{m1})} & \frac{f(g_1 \cap w_2)}{\sum_{m=1}^q f(w_{m2})} & \dots & \frac{f(g_1 \cap w_r)}{\sum_{m=1}^q f(w_{mr})} \\ \frac{f(g_2 \cap w_1)}{\sum_{m=1}^q f(w_{m1})} & \frac{f(g_2 \cap w_2)}{\sum_{m=1}^q f(w_{m2})} & \dots & \frac{f(g_2 \cap w_r)}{\sum_{m=1}^q f(w_{mr})} \\ \vdots & \vdots & \ddots & \vdots \\ \frac{f(g_m \cap w_1)}{\sum_{m=1}^q f(w_{m1})} & \frac{f(g_m \cap w_2)}{\sum_{m=1}^q f(w_{m2})} & \dots & \frac{f(g_m \cap w_r)}{\sum_{m=1}^q f(w_{mr})} \end{bmatrix} \quad (9)$$

Fig. 4 depicts the joint probability distribution for a given geographical region derived using (9). The elements in (9) indicate the likelihood that a specific set of solar irradiance and wind speed will occur. Similarly, each point on the joint probability distribution curve represents the probability corresponding to different weather scenarios. The higher values correspond to the scenarios occurring more frequently, whereas lower values denote less frequent scenarios. Thus, joint probability distribution matrix in the protection algorithm enables the consideration of any correlation between solar irradiance and wind speed, utilizing meteorological data. It shall be noted that, the number of fault scenarios considered during dataset generation have been simulated considering the joint probability distribution matrix including changes in both renewable sources (i.e. solar irradiance and wind speed). The integration of the joint probability distribution approach into the hybrid microgrid protection framework using STGCN will be described in the subsequent section.

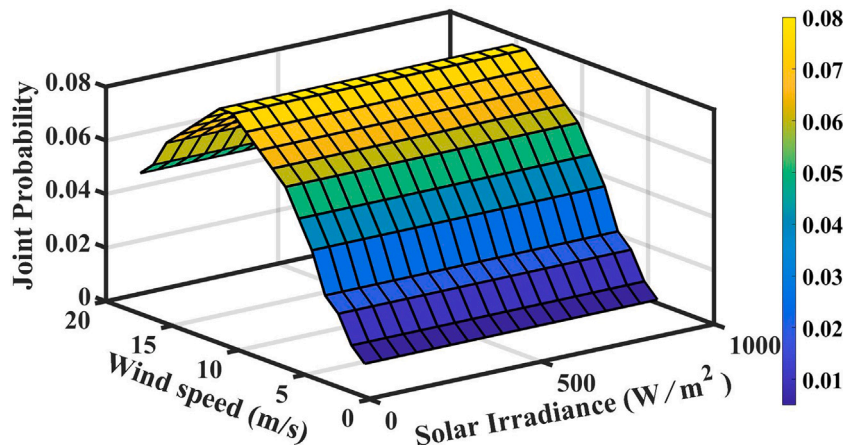


Fig. 4. Solar-Wind Joint Probability Distribution.

5. Proposed STGCN-based hybrid microgrid protection scheme

Development of STGCN-based hybrid microgrid protection scheme with resiliency to N-1 contingency and renewable intermittency will be discussed in this section. This approach enables more accurate predictions and facilitates the implementation of enhanced protection measures.

5.1. Overview of GNN

In this subsection, the basic graph structure along with graph-related terminology and definitions are presented followed by brief introduction to GCN and STGCN.

5.1.1. Graph structure

Let's consider a graph $G = (\mathcal{V}, \mathcal{E})$, where \mathcal{V} represents the set of vertices (nodes) and \mathcal{E} represents the set of edges. Each node $v_i \in \mathcal{V}$ is associated with a feature vector $\mathcal{V} = \{v_1, v_2, \dots, v_B\}$, while each edge $e_{ij} = (v_i, v_j) \in \mathcal{E}$ denotes the connection between the nodes v_i and v_j . A typical graph structure can be described by an adjacency matrix $\mathcal{A} \in \mathcal{R}^{B \times B}$ and degree matrix $\mathcal{D} \in \mathcal{R}^{B \times B}$, where B is the total number of nodes, $B = |\mathcal{V}|$. The adjacency matrix for the undirected graph is defined as [32],

$$\mathcal{A}_{ij} = \begin{cases} 1 & v_i, v_j \in \mathcal{E} \text{ and } i \neq j \\ 0 & \text{otherwise} \end{cases} \quad (10)$$

The elements of (10) represent the connection between nodes v_i and v_j . The degree matrix is diagonal and can be represented as,

$$D_{ii} = \sum_{j=1}^B \mathcal{A}_{ij} \quad (11)$$

A graph also possesses nodal features/attributes given by nodal feature matrix $\mathcal{X} \in \mathcal{R}^{B \times F}$, where F is the dimension of nodal feature matrix. In general, a graph structure is alternatively given by the Laplacian matrix \mathcal{L} as [32],

$$\mathcal{L} = \mathcal{D} - \mathcal{A} \quad (12)$$

5.1.2. GCN

GCNs represent a type of GNN that combines graph theory with the intrinsic convolutional operations of convolutional neural networks (CNNs) to execute graph data processing tasks. GCNs can extract both spectral and spatial characteristics, hence they are classified as either spectral-based GCNs or spatial-based GCNs [31]. The nodes in the GCN update their features using convolutional layer which is defined as,

$$\mathcal{X}^{(k+1)} = \text{ReLU}(\hat{\mathcal{A}} \mathcal{X}^k \mathcal{W}^k) \quad (13)$$

where $\text{ReLU}(\cdot)$ is an activation function, \mathcal{X}^k is the input matrix with feature information at k th layer, \mathcal{W}^k is the learnable GCN weight matrix at k th layer and $\hat{\mathcal{A}}$ is a self-normalized adjacency matrix derived from \mathcal{A} expressed as,

$$\hat{\mathcal{A}} = \tilde{\mathcal{D}}^{-\frac{1}{2}} \tilde{\mathcal{A}} \tilde{\mathcal{D}}^{-\frac{1}{2}} \quad (14)$$

where $\tilde{\mathcal{A}} = \mathcal{A} + \mathcal{I}$, and \mathcal{I} denotes identity matrix, $\tilde{\mathcal{D}}_{ii} = \sum_j \tilde{\mathcal{A}}_{ij}$.

This self-normalized adjacency matrix $\hat{\mathcal{A}}$ determines how information flows across the graph during convolutional operations. Similarly, a parameterised weight matrix \mathcal{W}^k for feature mapping facilitates the transformation of input node features into a higher-dimensional space. This process effectively captures the intricate structural patterns and relationships inherent in the graph data. However, GCNs have a single

adjacency matrix that depicts the static graph topology. This limits their ability to effectively capture temporal information and dynamic relationships within the data. Also, increasing the number of GCN layers, node features exhibit an average tendency known as over-smoothing. Hence, restrictions on the number of layers reduces GCN's capacity for feature recognition [30].

5.1.3. STGCN

A spatiotemporal convolutional block (ST-conv block) is a key component in STGCNs that is used to efficiently analyze spatiotemporal graph-structured input. Each ST-conv block is structured with two gated temporal convolution layers sandwiched between one spatial graph convolution layer. This block captures spatiotemporal dependencies and dynamics in graph-structured data using temporal graph convolutions and integrates information across different time steps, making it suitable for fault detection/classification tasks. The temporal convolution is given by,

$$\text{conv}_{a,b} = \sum_{i=1}^{uv} d_i w_i \quad (15)$$

where (a, b) denotes the size of input feature, uv represents the size of convolutional kernel, d signifies the weight of convolutional kernel, w represents the waveform feature, and i is the index for both the kernel weight and the feature. The computation of the output feature $\mathcal{X}_{T1}^{(k+1)}$ of the first temporal convolutional layer for the input $\mathcal{X}^{(k)}$ of the ST-conv block is as follows:

$$\mathcal{X}_{T1}^{(k+1)} = \phi \left(\text{ReLU} \left(h_{c1}^{(k+1)} + h_{c2}^{(k+1)} + h_{c3}^{(k+1)} \right) \right) \quad (16)$$

$$h_{c1}^{(k+1)} = \text{sigmoid} \left(\mathcal{X}^{(k)} * \mathcal{Y}_{c1}^{(k+1)} \right) \quad (17)$$

$$h_{c2}^{(k+1)} = \phi \left(\mathcal{X}^{(k)} * \mathcal{Y}_{c2}^{(k+1)} \right) \quad (18)$$

$$h_{c3}^{(k+1)} = \mathcal{X}^{(k)} * \mathcal{Y}_{c3}^{(k+1)} \quad (19)$$

where $\phi(\cdot)$ denotes batch normalization operation; $\mathcal{Y}_{c1}^{(k+1)}$, $\mathcal{Y}_{c2}^{(k+1)}$, and $\mathcal{Y}_{c3}^{(k+1)}$ represent convolutional kernels of identical shapes; $\text{ReLU}(\cdot)$ and $\text{sigmoid}(\cdot)$ denotes the activation functions; and operator $(*)$ signifies convolutional operation. Following the first temporal convolutional layer, the output feature of the spatial convolutional layer $\mathcal{X}_s^{(k+1)}$ is computed as follows,

$$\mathcal{X}_s^{(k+1)} = \text{ReLU} \left(\hat{\mathcal{A}} z^{(k+1)} \mathcal{W}_5^{(k+1)} \right) \quad (20)$$

$$z^{(k+1)} = z_1^{(k+1)} // z_2^{(k+1)} // z_3^{(k+1)} // z_4^{(k+1)} \quad (21)$$

$$z_1^{(k+1)} = \text{ReLU} \left(\mathcal{X}_{T1}^{(k+1)} \mathcal{W}_1^{(k+1)} + b_1^{(k+1)} \right) \quad (22)$$

$$z_2^{(k+1)} = \text{ReLU} \left(\mathcal{X}_{T1}^{(k+1)} \mathcal{W}_2^{(k+1)} + b_2^{(k+1)} \right) \quad (23)$$

$$z_3^{(k+1)} = \text{ReLU} \left(\mathcal{X}_{T1}^{(k+1)} \mathcal{W}_3^{(k+1)} + b_3^{(k+1)} \right) \quad (24)$$

$$z_4^{(k+1)} = \text{ReLU} \left(\mathcal{X}_{T1}^{(k+1)} \mathcal{W}_4^{(k+1)} + b_4^{(k+1)} \right) \quad (25)$$

where $\mathcal{W}_1^{(k+1)}$, $\mathcal{W}_2^{(k+1)}$, $\mathcal{W}_3^{(k+1)}$, $\mathcal{W}_4^{(k+1)}$, $\mathcal{W}_5^{(k+1)}$ and $b_1^{(k+1)}$, $b_2^{(k+1)}$, $b_3^{(k+1)}$, $b_4^{(k+1)}$ are the learnable parameters; the operator $(//)$ signifies feature splicing which allows combining features from different layers.

Following, the spatial convolutional layer, the output feature $\mathcal{X}^{(k+1)}$ of the second temporal convolutional layer is given by,

$$\mathcal{X}^{(k+1)} = \phi \left(ReLU \left(h_{s_1}^{(k+1)} + h_{s_2}^{(k+1)} + h_{s_3}^{(k+1)} \right) \right) \quad (26)$$

$$h_{s_1}^{(k+1)} = \text{sigmoid} \left(\mathcal{X}_s^{(k+1)} * \mathcal{Y}_{s_1}^{(k+1)} \right) \quad (27)$$

$$h_{s_2}^{(k+1)} = \phi \left(\mathcal{X}_s^{(k+1)} * \mathcal{Y}_{s_2}^{(k+1)} \right) \quad (28)$$

$$h_{s_3}^{(k+1)} = \mathcal{X}_s^{(k+1)} * \mathcal{Y}_{s_3}^{(k+1)} \quad (29)$$

where $\mathcal{Y}_{s_1}^{(k+1)}$, $\mathcal{Y}_{s_2}^{(k+1)}$, and $\mathcal{Y}_{s_3}^{(k+1)}$ represent convolutional kernels of identical shapes.

5.2. Graph structure in microgrid system

As mentioned earlier, accurate fault diagnosis in the proposed hybrid microgrid system requires incorporating topological information along with the voltage and current measurements collected from sensors installed at the buses. In this regard, STGCN can effectively establish the relationship between buses (nodes) and distribution lines (edges). It also embeds them in the protection algorithm to carry out fault detection/classification and faulty line identification. In the present work, only node (bus) features i.e. the voltages and the currents corresponding to critical buses, have been taken into consideration. The use of information from only the critical sensors allows for reducing the dimension of the feature vector used for the classifier without sacrificing network observability. The feature information i.e. the current I and voltage V measurements obtained from sensors installed at the i th critical bus can be given by,

$$\mathcal{N}_{(I_i, V_i)} = (I_{i1}, V_{i1}, I_{i2}, V_{i2}, I_{i3}, V_{i3}) \in \mathcal{R} \quad (30)$$

where $i1$, $i2$, and $i3$ correspond to three phases in a three-phase system at i th bus.

The objective of the proposed protection scheme is to detect the faulty scenario, classify the fault type and also identify the faulty line using the feature information obtained from the sensors and physical connection between the buses of the microgrid network. The generalised objective function for the proposed fault diagnostic model can be framed as,

$$\mathcal{N}_{(FD/C, FZ)} = F(\mathcal{Z}, \mathcal{N}_{(I, V)}) \quad (31)$$

where \mathcal{Z} denotes the physical connection between the buses and updates the features in the graph convolutional layer.

5.3. Framework of STGCN-based protection scheme

The framework of the proposed STGCN-based protection scheme with resiliency against N-1 contingency and weather intermittency has been illustrated in Fig. 5. The protection algorithm initiates with the CSI task for acquiring the current and voltage measurements from certain optimal buses using observability analysis. Following a comprehensive observability analysis, the information from the buses 2, 4, 6, 9, 10, 11, 13, 14, 16 and 17 is found to be sufficient to maintain the observability of the complete system during normal and N-1 contingency scenarios.

Following the CSI task, joint probability distribution matrix (9) is estimated considering the correlation between solar irradiance and wind speed historical data. Furthermore, the dataset generation is carried out for the proposed hybrid microgrid model in MATLAB/Simulink using joint probability distribution with a wide variation in operating scenarios and fault parameters. Finally, the feature information obtained from the sensors and the topological information of the microgrid network

is input to the STGCN classifier modules for performing the protection tasks, i.e. to detect/classify faults and to identify the faulty line.

For the proposed work, two independent STGCN classifier modules are designed to perform fault detection/classification (FD/C) and faulty line identification (FZ). When the fault occurs in the microgrid network, the impact of fault at a particular bus depends upon the physical distance between the faulty line and the bus where the fault waveform is measured. Thus, faults have a greater impact on the buses directly connected to the faulty lines, so that faulty line identification becomes more dependent on microgrid network topology information. However, fault type classification relies mostly on the feature information obtained from fault waveforms. A common ST-conv block which extracts the basic feature information necessary for executing protection tasks, is implemented as shown in Fig. 6. Additionally, two separate ST-conv blocks are constructed to aggregate the fault features required for FDC and FZ tasks. Using these two ST-conv blocks, two distinct classifiers are developed. Inclusion of the possibility of N-1 contingency during CSI formulation and during dataset generation allows for accurate fault detection/classification and faulty line identification even during single sensor loss and single line outage, without any additional classifier module.

In the proposed model, the feature input data shape is (17, 241, 60), where 17 indicates the number of buses in the network, 241 represents the number of samples and 60 denotes the distinct features acquired from critical sensors. The fault detection/classification task can be regarded as a 12-class classification task with labels as A-G, B-G, C-G, AB, BC, AC, AB-G, BC-G, AC-G, ABC, ABC-G and NF corresponding to 11 types of faults and one no-fault scenario. Similarly, the faulty line identification task can be regarded as a 14-class classification task with labels Z1, Z2, Z3, Z4, Z5, Z6, Z7, Z8, Z9, Z10, Z11, Z12, Z13 and Z14 corresponding to 14 number of lines in the microgrid system.

6. Performance analysis

The efficacy of the proposed STGCN-based protection scheme has been evaluated in a hybrid microgrid system, demonstrating its ability to adapt to variations in network topology and weather fluctuations using the information from sensors installed at critical buses. Considering the entire variation in the range of fault parameters, weather attributes, possible fault types, types of DERs disconnected and loading conditions resulted in a total dataset comprising of 275,968 cases for the fault class and 784 cases for the no-fault class. Each case of the dataset corresponds to a particular operating/fault condition of the microgrid being represented by the simulated voltage and current waveforms. The dataset consisting of 276,752 cases (fault and no-fault) has been randomly split into training and testing data with a training/testing ratio of 75%/25%. Thus, the training dataset consists of 75% of the samples (275,968 fault cases and 784 no-fault cases), while the testing dataset comprises the remaining 25% of the samples (68,992 fault cases and 196 no-fault cases). To avoid possible overfitting during training, care was taken to maintain diversity in the dataset. The scheme has been validated for 68,992 faulty scenarios corresponding to distribution line faults considering all possible single line and sensor outages with wide variations in fault types, fault parameters i.e. fault resistance (R_f), fault inception angle (θ_f), fault location (L_f) and operating parameters i.e. solar irradiance (g), wind speed (w). In addition to this, 196 non-faulty scenarios have been simulated with wide variation in loading conditions i.e. $\pm 5\%$ to $\pm 40\%$ in steps of 5%. The variation in fault and operating parameters carried out for simulating faulty scenarios and variation in loading conditions for non-faulty dataset is shown in Table 1.

The performance of each STGCN classifier module has been analyzed in terms of its effectiveness in performing fault detection/classification (FD/C module) and faulty section identification (FZ module). In addition to accuracy, the performance of the classifier modules (FD/C and FZ) has been quantified in terms of the standard reliability indices i.e. dependability and security. Also, the performance of the proposed scheme

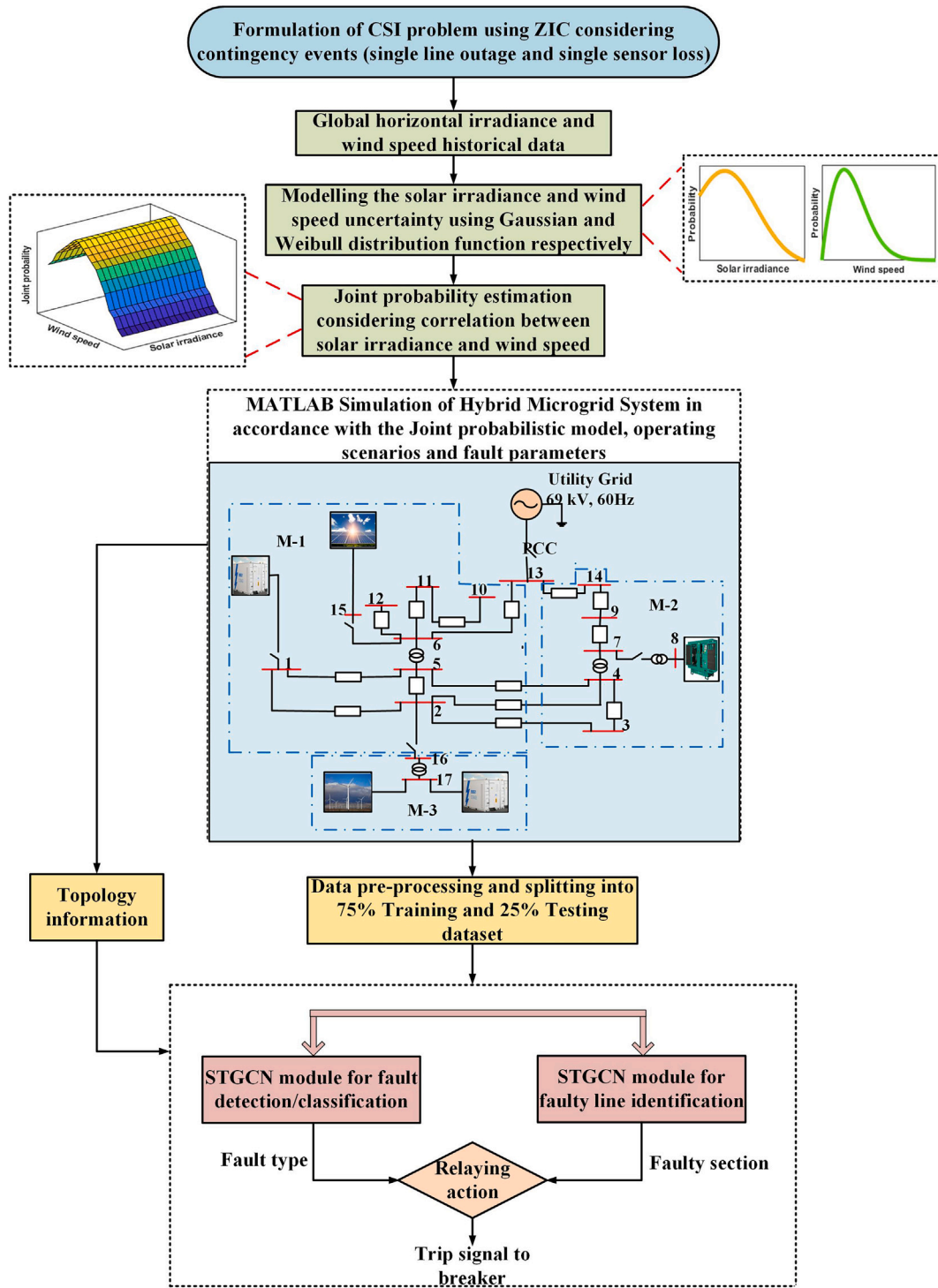


Fig. 5. Flowchart of STGCN based microgrid protection scheme.

has been evaluated for high resistance fault scenarios, different DER configurations, dynamic load variations, and different noise conditions.

6.1. STGCN module for fault detection/classification (FD/C)

In order to expedite relay response time and streamline the protection task, fault detection and classification are executed simultaneously utilizing a single module based on STGCN, known as FD/C module. The efficacy of the STGCN FD/C module has been analyzed for different types

of line faults occurring under normal as well as N-1 contingency scenarios. The details of the test cases and the fault wise performance analysis of FD/C module in terms of accuracy are described in Table 2. The proposed FD/C module is seen to accurately classify over 99.87 % of the test cases.

The performance comparison of the proposed STGCN-based scheme has also been carried out with GCN, long short-term memory (LSTM) and CNN classifiers as in Table 3 in terms of the reliability indices i.e. accuracy, dependability and security [33]. The increased level of accuracy,

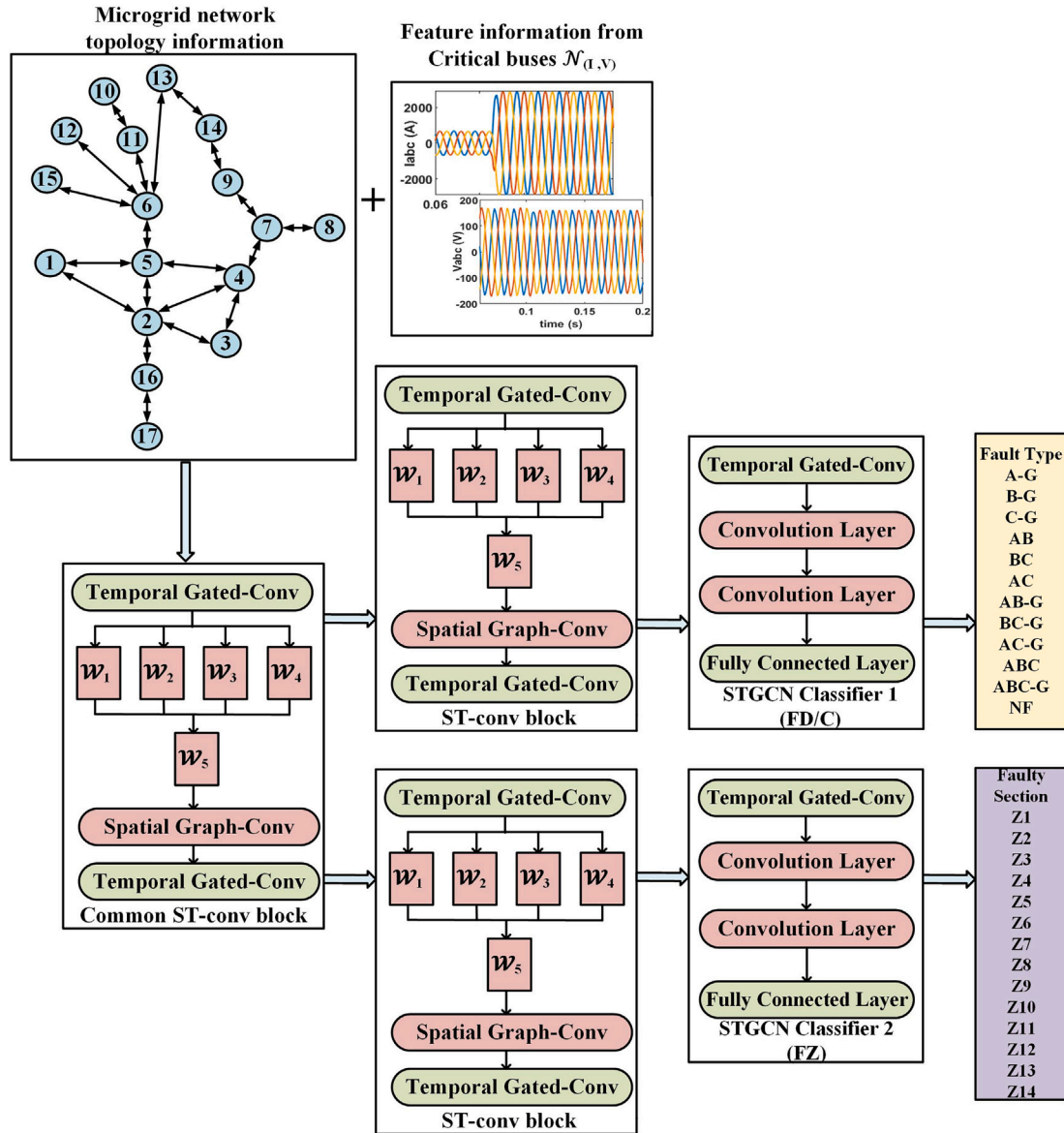


Fig. 6. Architecture of STGCN.

Table 1
Fault and operating parameters for dataset generation.

Fault scenario	Variation in fault and operating parameters considered	Number of scenarios	
		Training data	Testing data
Faulty	Fault types- A-G, B-G, C-G, AB, AC, BC, AB-G, BC-G, AC-G, ABC, ABC-G Fault resistances $R_f = 0.01-100\Omega$ Fault inception angles $\theta_f = 0-90^\circ$ Fault locations $L_f = 0-6 \text{ km}$ Faulty lines- Z1, Z2, Z3, Z4, Z5, Z6, Z7, Z8, Z9, Z10, Z11, Z12, Z13, Z14 Global horizontal irradiance, $g = 100-1000 \text{ W/m}^2$ Wind speed, $w = 2-20 \text{ m/s}$ DER outages- solar outage, wind outage, DG outage	206,976	68,992
Non-faulty	Load variation in the range of $\pm 5\%$ to $\pm 40\%$ in steps of 5%	588	196

Table 2
Performance of STGCN-based FD/C module for different fault types.

Type of fault		Actual test cases	Accurately predicted test cases	Misclassified test cases	Accuracy of FD/C (%)	Overall accuracy (%)
Single-phase-G	A-G	6272	6269	3	99.95	99.87
	B-G	6272	6270	2	99.97	
	C-G	6272	6270	2	99.97	
Phase-phase	AB	6272	6268	4	99.94	
	BC	6272	6267	5	99.92	
	AC	6272	6268	4	99.94	
Two-phase-G	AB-G	6272	6267	5	99.92	
	BC-G	6272	6262	10	99.85	
	AC-G	6272	6264	8	99.87	
Three-phase	ABC	6272	6260	12	99.81	
Three-phase-G	ABC-G	6272	6243	29	99.54	
No fault	NF	196	195	1	99.49	

Table 3
Reliability analysis.

Protection schemes	Accuracy (%)	Dependability (%)	Security (%)
STGCN	99.87	99.88	99.49
GCN	99.07	99.07	98.98
LSTM	98.78	98.78	98.47
CNN	97.54	97.54	98.47

dependability and security obtained is attributed to the effectiveness of the STGCN classifier in capturing deeper structural information along with the fault features. A high value of dependability and security relates to providing tripping only when intended (during faults) and avoiding false alarms (during healthy cases) respectively under various contingency and weather intermittency scenarios. In order to showcase the effectiveness of the proposed classifier in dealing with fluctuations in solar irradiance and wind speed, the accuracy of the FD/C module using 3-D plot has been depicted in Fig. 7. The 3-D plot is generated by assessing the effectiveness of the STGCN classifier, which accurately categorizes fault scenarios under varying levels of solar irradiance and wind speed. The scheme achieves a classification accuracy above 97.5 % across the entire range of dataset considered in the study, with notably superior performance observed for $g > 200 \text{ W/m}^2$ and $w > 5 \text{ m/s}$.

Additionally, certain prototypical scenarios to assess the suitability of the proposed approach in executing necessary relay response during weather intermittency are simulated. One such scenario corresponding to low irradiance level $g = 700 \text{ W/m}^2$ followed by A-G fault in

section Z1 at $t = 0.1002 \text{ s}$ is depicted in Fig. 8. Fig. 8(a) illustrates the variation in current waveform acquired at bus B-2 during fluctuations in irradiance level and occurrence of a fault. Fig. 8(b) shows the response of STGCN classifier for scenario in Fig. 8(a). It can be observed that despite the reduced irradiance level, the proposed scheme is able to provide the necessary relay response within 11.47 ms of fault inception.

6.2. STGCN module for faulty line identification (FZ)

In the event of a fault, it is essential that the faulty section is isolated and the supply is restored as soon as possible to minimize its impact. In this sub-section, the efficacy of the STGCN-based faulty line identification module (FZ) has been validated in terms of its ability to accurately identify the faulty section in the microgrid system during normal and contingency scenarios. The FZ module has been validated with the test cases simulated by considering variations in parameters mentioned in Table 1. The accuracy of the section identification unit is depicted in Table 4. In comparison with GCN, LSTM and CNN classifier modules, STGCN-based FZ module demonstrates an increased accuracy of 99.88 %, indicating resiliency to weather changes and N-1 contingencies.

The accuracy results reported in Table 4 has been obtained by implementing the classifiers on the same dataset for the microgrid model of Fig. 1, while considering N-1 contingency. For the sake of uniform comparison, same training and testing dataset (Table 1) has been considered for all the classifiers in Table 4.

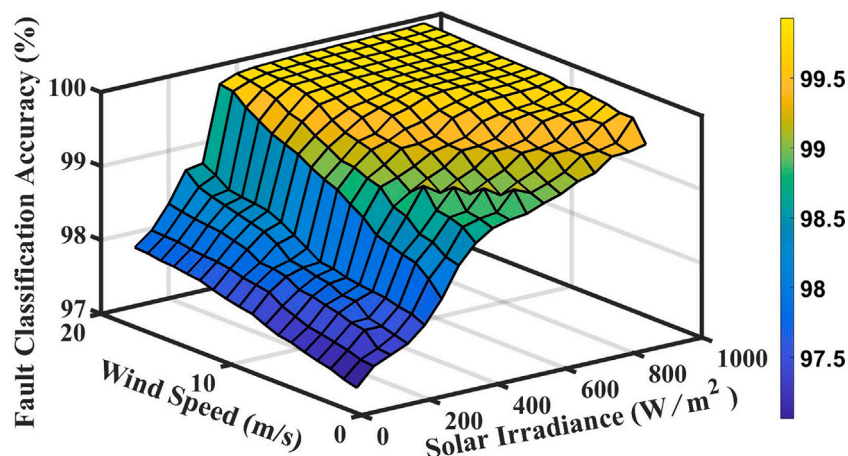
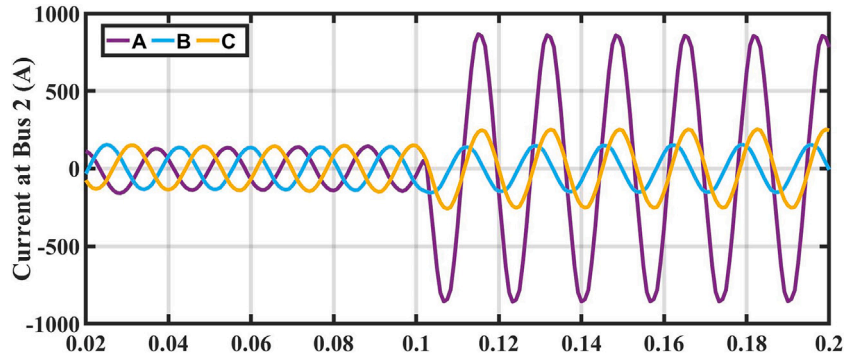
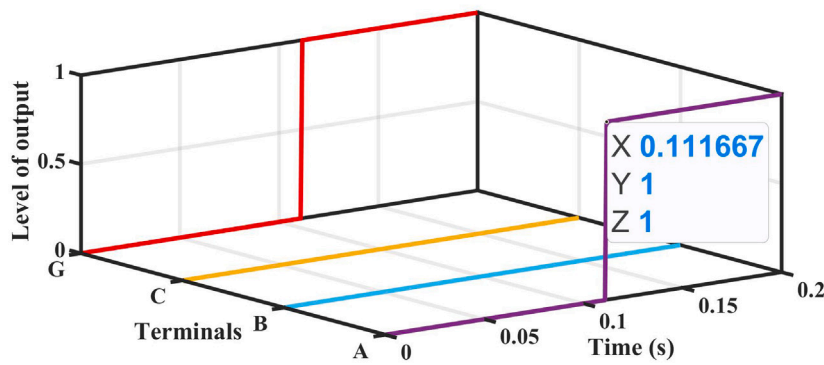


Fig. 7. Fault detection/classification accuracy of STGCN classifier under varying wind speed and solar irradiance.



(a)



(b)

Fig. 8. Low solar irradiance ($g = 700 \text{ W/m}^2$) scenario followed by A-G fault in section Z1 at $t = 0.1002 \text{ s}$ (a) Current waveform acquired at bus B-2 (b) Response of STGCN-based FD/C module.

Table 4

Performance of STGCN-based FZ module for identifying faults in different sections.

Accuracy of faulty line identification module (FZ)					
Faulty section	No. test cases	STGCN	GCN	LSTM	CNN
Z1	4928	99.90	99.05	97.63	94.78
Z2	4928	99.88	99.01	97.85	95.58
Z3	4928	99.88	98.88	97.48	95.37
Z4	4928	99.92	98.94	97.48	95.58
Z5	4928	99.90	98.70	97.52	94.83
Z6	4928	99.90	98.62	97.35	94.73
Z7	4928	99.86	98.60	97.48	94.56
Z8	4928	99.84	98.88	97.71	94.56
Z9	4928	99.88	98.84	97.66	95.62
Z10	4928	99.90	98.60	97.69	95.40
Z11	4928	99.88	98.60	97.21	94.32
Z12	4928	99.84	98.90	97.42	95.70
Z13	4928	99.84	99.01	97.40	94.36
Z14	4928	99.88	99.01	97.40	94.93
Overall accuracy (%)	–	99.88	98.83	97.52	95.02

6.3. Performance during high fault resistance scenarios

Detection of faults with high fault resistance is a challenge because the insignificant increase in the fault current may not be sufficient to trigger the relaying scheme. Despite the fact that, there is no significant damage caused by low-magnitude fault currents, energized conductors can induce arcing, resulting in fires. As such, early diagnosis of high resistance faults is crucial. The scenario is more relevant during islanding conditions. In this regard, the effectiveness of

the proposed scheme has been analyzed against fault scenarios with high fault resistances ($R_f = 100\text{--}200 \Omega$) by considering wide variation in operating parameters i.e. solar irradiance and wind speed and line outages as shown in Table 5. It can be observed that in spite of the reduced solar irradiance and wind speed levels for some of the cases depicted in Table 5, the proposed scheme exhibits high selectivity against high fault resistance scenarios even during line outages.

Table 5
Response of STGCN-based protection scheme for high fault resistance scenarios.

High resistance fault scenarios						Response of STGCN-based protection scheme		
Faulty line (Line outage)	Fault parameters			Operating parameters		Output of FD/C module	Output of FZ module	Relay response (ms)
	R_f (Ω)	θ_f (deg.)	L_f (km)	g (W/m ²)	w (m/s)			
A-G in Z7 (Z3 outage)	130	90	0.05	600	9	A-G	Z7	15.2
B-G in Z4 (No outage)	120	0	0.3	650	5	B-G	Z4	14.9
C-G in Z6 (Z1 outage)	175	90	0.2	700	13	C-G	Z6	15.7
AB-G in Z3 (Z2 outage)	150	90	0.1	450	7	AB-G	Z3	16
BC-G in Z8 (Z14 outage)	200	0	1.5	900	11	BC-G	Z8	15.8
AC-G in Z10 (Z11 outage)	185	90	4	850	16	AC-G	Z10	16.2
ABC-G in Z14 (Z8 outage)	115	0	1.8	500	16	ABC-G	Z14	16.5

Table 6
Response of STGCN-based protection scheme for dynamic load variations.

Input parameters				Response of STGCN classifier		
Fault type	Fault parameters	Operating parameters	Variation in loading	FD/C output	FZ output	Relaying action (relay response)
Faulty scenarios						
ABC-G in Z4	$R_f = 1\Omega$, $\theta_f = 90^\circ$, $L_f = 0.2$ km	$g = 600$ W/m ² , $w = 12$ m/s	+40 % in L-4	ABC-G	Z4	Trip signal to terminals a, b and c (13.7 ms)
AC-G in Z1	$R_f = 0.1\Omega$, $\theta_f = 90^\circ$, $L_f = 0.1$ km	$g = 700$ W/m ² , $w = 11$ m/s	-30 % in L-2	AC-G	Z1	Trip signal to terminals a and c (12.4 ms)
B-G in Z8	$R_f = 0.01\Omega$, $\theta_f = 90^\circ$, $L_f = 1$ km	$g = 500$ W/m ² , $w = 9$ m/s	+35 % in L-9	B-G	Z8	Trip signal to terminal b (12.8 ms)
Non-faulty scenarios						
Load variation	-	$g = 650$ W/m ² , $w = 8$ m/s	-40 % in L-3	NF	EXT	No action
Load variation	-	$g = 800$ W/m ² , $w = 14$ m/s	+20 % in L-10	NF	EXT	No action

6.4. Performance for dynamic load variations

During operations, microgrids undergo wide variations in the linear and non-linear loads. The similarity in voltage/current profiles occurring due to load variations and distribution line faults often results in maloperation of relays. The ability of the protection scheme to avoid unnecessary tripping during abrupt variations in loading conditions has been evaluated in this section. For the sensor information acquired from the relaying buses during load variation up to ± 40 %, the response of the protection scheme is reported in Table 6. In addition of correctly distinguishing between load encroachment and fault, the proposed scheme is able to execute the fault detection task promptly within one cycle.

6.5. Performance under different noise conditions

The current and voltage measurements at the relaying buses are often contaminated with noise resulting in unintended tripping of relays. To test the immunity of the proposed protection scheme against noisy signals, the current and voltage signals obtained from the critical sensors are intentionally mixed with white Gaussian noise (WGN) having signal-to-noise ratio (SNR) in the range of 20–40 dB [34]. The performance of the protection scheme decreases with lower values of SNR. A few random test cases have been contaminated with different levels of SNRs to check the effectiveness of the scheme with adaptiveness to

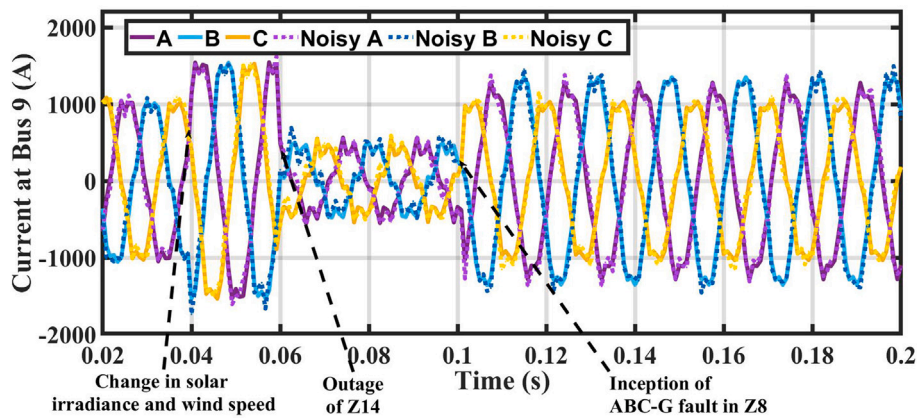
N-1 contingency (i.e. both line and DER outages) scenarios with wide variation in solar irradiance and wind speed as shown in Table 7. Fig. 9 shows the performance of STGCN classifier for a scenario corresponding to varying irradiance level and wind speed followed by outage of line Z14 and ABC-G fault in line Z8 at $t = 0.1002$ s with 25 dB WGN. Fig. 9(a) depicts three phase current waveform at bus B-9. Fig. 9(b) shows the output of STGCN classifier and trip signal generation within 16.47 ms for noisy signal.

6.6. Comparison of STGCN approach with reported protection algorithms

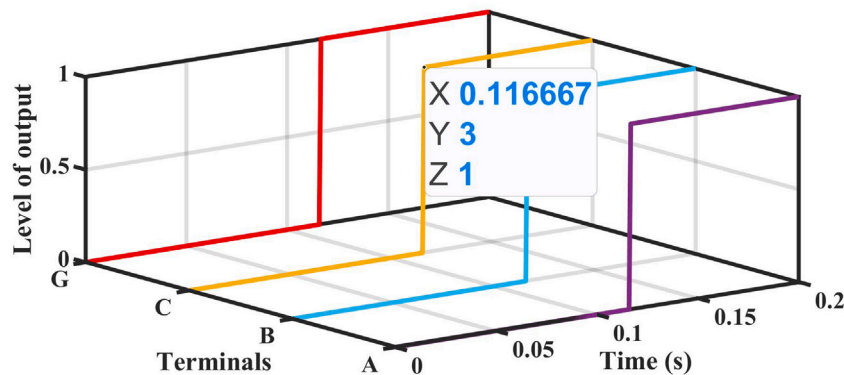
The proposed STGCN-based protection algorithm has been evaluated for its robustness against uncertainties in solar irradiance and wind speed. This evaluation involved a thorough comparison with other state-of-the-art microgrid protection algorithms reported in the literature [18,19,35] using joint probability distribution approach. The comprehensive comparison illustrated in Table 8 is based on several parameters such as the microgrid system, protection algorithm, inclusion of network topology information during the training, line and sensor outages, formulation of CSI task, robustness against noise, and protection tasks performed. The comparative analysis carried out reveals that the proposed protection approach offers improved immunity against weather intermittency and N-1 contingency scenarios resulting from both line outages and sensor failures.

Table 7
Performance of STGCN-based protection scheme under different noise conditions.

Fault type	Faulty zone	Fault parameters	Line/DER outage	g (W/s^2)	w (m/s)	SNR (dB)	Relay response (ms)
B-G	Z5	$R_f = 0.1\Omega$, $\theta_f = 0^\circ$, $L_f = 0.2$ km	Z1 line	450	9	30	15.6
ABC-G	Z2	$R_f = 0.01\Omega$, $\theta_f = 90^\circ$, $L_f = 0.15$ km	solar DER	-	12	20	15.3
ABC	Z11	$R_f = 1\Omega$, $\theta_f = 90^\circ$, $L_f = 2$ km	No outage	600	10	25	13.2
C-G	Z3	$R_f = 0.1\Omega$, $\theta_f = 0^\circ$, $L_f = 0.1$ km	Wind DER	700	-	35	14.9
BC-G	Z8	$R_f = 0.001\Omega$, $\theta_f = 90^\circ$, $L_f = 1.8$ km	Z7 line	550	13	40	12.6



(a)



(b)

Fig. 9. Performance of STGCN classifier for varying solar irradiance and wind speed followed by outage of line Z14 and ABC-G fault in line Z8 at $t=0.1002$ s (a) Three phase current at bus B-9 (b) Trip signal generation for faulty signal in (a) contaminated with 25 dB WGN within 16.47 ms.

Table 8
Comparison of proposed STGCN approach with other protection algorithms.

Parameters of comparison	Microgrid protection algorithms using joint probability distribution approach to model the uncertainty in solar and wind DERs			
	[18]	[35]	[19]	Proposed approach
Microgrid system considered	AC microgrid	AC microgrid	DC microgrid	Hybrid microgrid
Protection algorithm adopted	Wavelet transform and Rotation forest classifier	Wavelet transform and Random forest classifier	CNN classifier	STGCN classifier
Network topology information embedded during the training	No	No	No	Yes
Line outages considered	No	No	No	Yes
Sensor loss considered	No	No	No	Yes
Formulation of CSI task for sensor installation	Not considered	Not considered	Not considered	Considered
Robustness against noisy signals	Not considered	Not considered	Not considered	Considered
Protection tasks performed	FD/C and FZ* with resilience against weather intermittency	FD/C and FZ* with resilience against weather intermittency	FD/C and FZ* with resilience against weather intermittency and DER outages	FD/C and FZ* with resilience against weather intermittency and N-1 contingency (both line and sensor outages)

* FD/C-Fault detection/classification, FZ-Faulty line identification.

7. Conclusion

A novel scalable protection framework for hybrid microgrids aimed at improving fault detection/classification accuracy with enhanced resilience against contingency scenarios and weather intermittency is proposed in this work. In this context, the CSI task is formulated as an optimization problem aimed at achieving full system observability under both normal and contingency events. The concept of ZIC is incorporated which results in considerable reduction in sensor installation costs and enhanced measurement redundancy for single line outage and single sensor loss contingency. To accommodate intermittency and potential correlations between solar irradiance and wind speeds, a joint probability distribution approach, encompassing the uncertainty present in both variables is adopted. With the feature information derived from critical sensors and the network topology information of the microgrid system, a set of STGCN classifier modules has been developed to perform the protection tasks. The high accuracy of 99.87 % achieved by the proposed scheme for fault detection/classification and faulty section identification is attributed to the effectiveness of the STGCN classifier modules in embedding the network topology information during the training and hence perform accurate mapping in high-dimensional space. The effectiveness of the proposed scheme is also reflected by the high degree of dependability (99.88 %) and security (99.49 %) attained for the protection tasks.

CRedit authorship contribution statement

Goyal Ramesh Rao Awagan: Writing – review & editing, Writing – original draft, Visualization, Validation, Software, Methodology, Formal analysis, Data curation, Conceptualization. **Jing Jiang:** Writing – review & editing, Supervision, Project administration, Funding acquisition, Formal analysis. **Ebha Koley:** Validation, Supervision, Formal analysis, Conceptualization. **Subhojit Ghosh:** Writing – review & editing, Supervision, Investigation, Formal analysis, Conceptualization. **Pratik Harsh:** Writing – review & editing, Formal analysis. **Hongjian Sun:** Writing – review & editing, Supervision, Project administration, Funding acquisition.

Declaration of competing interest

The authors declare the following financial interests/personal relationships which may be considered potential competing interests:

Awagan Goyal Ramesh Rao reports that financial support was provided by Engineering and Physical Sciences Research Council. Jing Jiang and Hongjian Sun report that travel support was provided by European Union. If there are other authors, they declare that they have no known

competing financial interests or personal relationships that could have appeared to influence the work reported in this paper.

Acknowledgements

This work was supported by the Engineering and Physical Sciences Research Council [grant number EP/Y005376/1] – VPP-WARD Project (<https://www.vppward.com>). This work was also supported by the European Union's Horizon 2020 research and innovation programme under the Marie Skłodowska-Curie Grant Agreement No. 872172 TESTBED2 project.

Data availability

Data will be made available on request.

References

- [1] Shi W, Liang H, Bittner M. Dynamic microgrid formation for resilient distribution systems considering large-scale deployment of mobile energy resources. *Appl Energy* 2024;362:122978. doi:<https://doi.org/10.1016/j.apenergy.2024.122978>.
- [2] Wang C, Yan J, Marnay C, Djilali N, Dahlquist E, Wu J, et al. Distributed energy and microgrids (DEM). *Appl Energy* 2018;210:685–89. doi:<https://doi.org/10.1016/j.apenergy.2017.11.059>.
- [3] Beheshtaein S, Cuzner R, Savaghebi M, Guerrero JM. Review on microgrids protection. *IET Gener Transm Dis* 2019;13:743–59. doi:<https://doi.org/10.1049/iet-gtd.2018.5212>.
- [4] Mirsaeidi S, Dong X, Said DM. Towards hybrid AC/DC microgrids: critical analysis and classification of protection strategies. *Renew Sustain Energy Rev* 2018;90:97–103. doi:<https://doi.org/10.1016/j.rser.2018.03.046>.
- [5] Feng W, Jin M, Liu X, Bao Y, Marnay C, Yao C, et al. A review of microgrid development in the United States—a decade of progress on policies, demonstrations, controls, and software tools. *Appl Energy* 2018;228:1656–68. doi:<https://doi.org/10.1016/j.apenergy.2018.06.096>.
- [6] Núñez-Mata O, Palma-Behnke R, Valencia F, Urrutia-Molina A, Mendoza-Araya P, Jiménez-Estévez G. Coupling an adaptive protection system with an energy management system for microgrids. *Electr J* 2019;32:106675. doi:<https://doi.org/10.1016/j.jtejt.2019.106675>.
- [7] Sarangi S, Sahu BK, Rout PK. Distributed generation hybrid AC/DC microgrid protection: a critical review on issues, strategies, and future directions. *Int J Energy Res* 2020;44:3347–64. doi:<https://doi.org/10.1002/er.5128>.
- [8] Tiwari SP, Koley E, Ghosh S. Communication-less ensemble classifier-based protection scheme for DC microgrid with adaptiveness to network reconfiguration and weather intermittency, sustainable Energy. *Grids Networks* 2021;26:100460. doi:<https://doi.org/10.1016/j.segan.2021.100460>.
- [9] Ramesh Rao AG, Koley E, Ghosh S. An optimal sensor location based protection scheme for DER-integrated hybrid AC/DC microgrid with reduced communication delay, sustainable Energy. *Grids Networks* 2022;30:100680. doi:<https://doi.org/10.1016/j.segan.2022.100680>.
- [10] Ramesh Rao AG, Koley E, Ghosh S. A LSTM-based approach for detection of high impedance faults in hybrid microgrid with immunity against weather intermittency and N-1 contingency. *Renew Energy* 2022;198:75–90. doi:<https://doi.org/10.1016/j.renene.2022.08.028>.

- [11] Manousakis NM, Korres GN. Optimal allocation of phasor measurement units considering various contingencies and measurement redundancy. *IEEE Trans Instrum Meas* 2019;69:3403–11. doi:<https://doi.org/10.1109/TIM.2019.2932208>.
- [12] Chen X, Wei F, Cao S, Soh CB, Tseng KJ. PMU placement for measurement redundancy distribution considering zero injection bus and contingencies. *IEEE Syst J* 2020;14:5396–406. doi:<https://doi.org/10.1109/JSYST.2020.2990435>.
- [13] Saleh KA, Zeineldin HH, El-Saadany EF. Optimal protection coordination for microgrids considering N – 1 contingency. *IEEE Trans Ind Inf* 2017;13:2270–78. doi:<https://doi.org/10.1109/TII.2017.2682101>.
- [14] Stasinou E-IE, Trakas DN, Hatziaziyriou ND. Microgrids for power system resilience enhancement, *ienergy*. 2022;1:158–69. doi:<https://doi.org/10.23919/IEEN.2022.0032>.
- [15] Aminifar F, Khodaei A, Fotuhi-Firuzabad M, Shahidehpour M. Contingency-constrained PMU placement in power networks. *IEEE Trans Power Syst* 2009;25:516–23. doi:<https://doi.org/10.1109/TPWRS.2009.2036470>.
- [16] Abdulrahman I, Radman G. ILP-based optimal PMU placement with the inclusion of the effect of a group of zero-injection buses. *J Control Autom Electr Syst* 2018;29:512–24. doi:<https://doi.org/10.1007/s40313-018-0389-4>.
- [17] Ye H, Tian C, Ge Y, Wu L. Revisit optimal PMU placement with full zero-injection cluster and redundancy sharing. *IEEE Trans Power Syst* 2024; doi:<https://doi.org/10.1109/TPWRS.2024.3453300>.
- [18] Manohar M, Koley E, Ghosh S. Stochastic weather modeling-based protection scheme for hybrid PV–wind system with immunity against solar irradiance and wind speed. *IEEE Syst J* 2020;14:3430–39. doi:<https://doi.org/10.1109/JSYST.2020.2964990>.
- [19] Prasad Tiwari S, Koley E, Manohar M, Ghosh S, Mohanta DK, Bansal RC. Enhancing robustness of DC microgrid protection during weather intermittency and source outage for improved resilience and system integrity. *Int Trans Electr Energy Syst* 2021;31:e13243. doi:<https://doi.org/10.1002/2050-7038.13243>.
- [20] Wu Z, Pan S, Chen F, Long G, Zhang C, Yu PS. A comprehensive survey on graph neural networks. *IEEE Trans Neural Netw Learn Syst* 2021;32:4–24. doi:<https://doi.org/10.1109/TNNLS.2020.2978386>.
- [21] Kandasamy LM, Jaganathan K. Intelligent fault diagnosis using deep learning for a microgrid with high penetration of renewable energy sources. *Electr Power Compon Syst* 2023;51:332–50. doi:<https://doi.org/10.1080/15325008.2023.2168091>.
- [22] Liao W, Bak-Jensen B, Pillai JR, Wang Y, Wang Y. A review of graph neural networks and their applications in power systems. *J Mod Power Syst Clean Energy* 2022;10:345–60. doi:<https://doi.org/10.35833/MPCE.2021.000058>.
- [23] Liao W, Yang D, Wang Y, Ren X. Fault diagnosis of power transformers using graph convolutional network. *CSEE J Power Energy Syst* 2021;7:241–49. doi:<https://doi.org/10.17775/CSEEJPES.2020.04120>.
- [24] Tong H, Qiu RC, Zhang D, Yang H, Ding Q, Shi X. Detection and classification of transmission line transient faults based on graph convolutional neural network. *CSEE J Power Energy Syst* 2021;7:456–71. doi:<https://doi.org/10.17775/CSEEJPES.2020.04970>.
- [25] Chen K, Hu J, Zhang Y, Yu Z, He J. Fault location in power distribution systems via deep graph convolutional networks. *IEEE J Sel Areas Commun* 2020;38:119–31. doi:<https://doi.org/10.1109/JSAC.2019.2951964>.
- [26] Pandey A, Mohanty SR. Graph convolutional network based fault detection and identification for low-voltage DC microgrid. *J Mod Power Syst Clean Energy* 2023;11:917–26. doi:<https://doi.org/10.35833/MPCE.2022.000251>.
- [27] Kipf TN, Welling M. Semi-supervised classification with graph convolutional networks. 2017; arXiv:1609.02907. <https://arxiv.org/abs/1609.02907>.
- [28] Verdona A, Scardapane S, Panella M. Explainable spatio-temporal graph neural networks for multi-site photovoltaic energy production. *Appl Energy* 2024;353:122151. doi:<https://doi.org/10.1016/j.apenergy.2023.122151>.
- [29] Huang L, Sun Y, Xu J, Gao W, Zhang J, Wu Z. Optimal PMU placement considering controlled islanding of power system. *IEEE Trans Power Syst* 2013;29:742–55.
- [30] National Renewable Energy Laboratory (NREL), U.S. Department of Energy. Available at <https://nserdb.nrel.gov/data-viewer>. [Accessed on 03/07/2024].
- [31] Krismanto AU, Mithulananthan N, Kamwa I. Oscillatory stability assessment of microgrid in autonomous operation with uncertainties. *IET Renew Power Gener* 2018;12:494–504. doi:<https://doi.org/10.1049/iet-rpg.2017.0579>.
- [32] Ortiz L, Orizondo R, Águila A, González JW, López GJ, Isaac I. Hybrid AC/DC microgrid test system simulation: grid-connected mode. *Heliyon* 2019;5:e02862. doi:<https://doi.org/10.1016/j.heliyon.2019.e02862>.
- [33] Chan F-C. Performance assessment and control of power system relaying. *IEEE Trans Power Del* 1989;4:986–94. doi:<https://doi.org/10.1109/61.25579>.
- [34] Li X, Dyško A, Burt GM. Traveling wave-based protection scheme for inverter-dominated microgrid using mathematical morphology. *IEEE Trans Smart Grid* 2014;5:2211–18. doi:<https://doi.org/10.1109/TSG.2014.2320365>.
- [35] Manohar M, Koley E, Ghosh S. Microgrid protection under weather uncertainty using joint probabilistic modeling of solar irradiance and wind speed. *Comput Electr Eng* 2020;86:106684. doi:<https://doi.org/10.1016/j.compeleceng.2020.106684>.